



# Impact of crystal defects on carrier transport properties in high-purity germanium crystals



Pradeep Chandra Palletti <sup>a</sup>, Uta Juda <sup>a</sup>, Palvan Seyidov <sup>a</sup>, Mike Pietsch <sup>a</sup>, Nadine Schüller <sup>b</sup>, Andreas Fiedler <sup>a</sup>, R. Radhakrishnan Sumathi <sup>a,\*</sup>

<sup>a</sup> Leibniz-Institut für Kristallzüchtung (IKZ), Max-Born Str. 2, 12489, Berlin, Germany

<sup>b</sup> Freiberg Instruments GmbH, Delfter Str. 6, 09599, Freiberg, Germany

## ARTICLE INFO

**Keywords:**  
 Semiconductor detector  
 High-purity Ge  
 Vacancy complexes  
 Dislocations  
 Mobility  
 Carrier lifetime

## ABSTRACT

High-purity germanium (HPGe) crystals grown by the Czochralski method in a hydrogen atmosphere were analyzed to study the impact of defects on electrical properties. Microwave-detected photoconductivity (MDP) measurements at room temperature (RT) revealed ring-shaped patterns on the wafers, showing radial variations in minority carrier lifetime (40 to 100  $\mu$ s). At 83 K, the carrier lifetimes were significantly reduced by a factor of three, showing more pronounced ring-shaped patterns. These patterns correlate well with dislocation densities mapped on the wafer using etch pit density (EPD) analysis. Regions with both high dislocation density and dislocation-free zones exhibit reduced lifetimes, indicating the presence of deep-level defects. Temperature-dependent Hall effect (TDH) measurements on *p*-type samples revealed defects with activation energies of 0.019, 0.065, 0.2, and 0.25 eV. In the *n*-type sample, a minority carrier trap at 0.34 eV was identified with the deep level transient spectroscopy (DLTS). The mobility in the *p*-type samples increased with decreasing temperature, showing the highest mobility at 77 K ( $46,000 \text{ cm}^2 \text{ V}^{-1} \cdot \text{s}^{-1}$ ), while the *n*-type samples showed fluctuating mobility. Combined analysis of MDP, EPD, TDH, and DLTS data highlights the role of both extended and point defects in limiting carrier lifetime and mobility in detector-grade HPGe crystals.

## 1. Introduction

Owing to its high carrier mobility, long carrier lifetime, very low concentration of electrically active impurities and defects, germanium (Ge)-based detectors are highly valued in gamma-ray spectroscopy for their superior energy resolution and detection efficiency. [1,2] To ensure optimal performance, high-purity Ge (HPGe) detectors require an exceptionally low net impurity concentration, typically in the order of  $10^{10} \text{ cm}^{-3}$  or lower. Such ultrahigh purity ensures a fully depleted active volume ( $\approx 2 \text{ cm}$ , which corresponds to the penetration depth of 1 MeV  $\gamma$ -ray photons), under moderate reverse bias (2260 V), and minimizes charge trapping during carrier drift. [3] In addition to purity, high carrier mobility and long carrier lifetime are the essential parameters, directly influencing the charge transport properties and overall detector efficiency. [4,5] These characteristics determine the ability of the detector to collect charge carriers before recombination or trapping occurs, which is critical for maintaining energy resolution and fast response. However, achieving such performance levels depends heavily on how

well defects in the crystal are controlled during the crystal growth process. A wide range of intrinsic and extrinsic defects, including vacancy-related complexes, impurity-vacancy centers (such as *E*-centers), and extended defects like dislocations, can act as deep-level traps or recombination centers, degrading both carrier lifetime and mobility. [6] These electrically active defects introduce mid-gap states that alter the charge neutrality condition and contribute to carrier scattering and trapping phenomena, thereby limiting the detector's operational efficiency.

Over the past several decades, extensive research has been dedicated to identifying and characterizing defects in HPGe crystals due to their detrimental impact on radiation detector performance. W. L. Hansen et al. [7] studied etch pit density in Ge crystals grown along the [111] direction under a hydrogen atmosphere and observed that ring-shaped regions depleted of etch pits often correlate with poor detector performance, typically found near the middle and tail end of the crystal. These regions may indicate high densities of unbound vacancies or vacancy clusters, as dislocation movement is vacancy-mediated. G. S. Hubbard

\* Corresponding author.

E-mail address: [radhakrishnan.sumathi@ikz-berlin.de](mailto:radhakrishnan.sumathi@ikz-berlin.de) (R.R. Sumathi).

et al. [8] used DLTS and Hall effect techniques to investigate dislocation-related defects in ultra-pure *p*-type Ge, revealing two acceptor levels at 0.02 eV and 0.04 eV in crystals with dislocation densities between  $8 \times 10^3 \text{ cm}^{-2}$  to  $1.5 \times 10^4 \text{ cm}^{-2}$ . Further studies have reported deep-level traps associated with vacancy-donor or vacancy-impurity complexes in irradiated *n*-type Ge. For instance, P. M. Mooney et al. [9] identified electron traps  $E_1 = E_C - 0.2 \text{ eV}$  and  $E_2 = E_C - 0.40 \text{ eV}$  and one-hole trap  $H_1 = E_V + 0.25 \text{ eV}$ , while N. Fukuoka et al. [10,11] confirmed similar levels. Upon annealing,  $E_2$  disappeared between 100 °C and 200 °C, while  $H_1$  annealed at 300 °C, coinciding with the appearance of a new hole trap ( $H_2$ ). The defect introduction rate increased tenfold as the doping concentration rose from  $3 \times 10^{13}$ – $3 \times 10^{14} \text{ cm}^{-3}$ . This correlation suggests that the observed defects may be related complexes involving vacancies (or interstitials) and donor impurities. K. Ito et al. [12] used DLTS to study defects in undoped Ge after hydrogen implantation and electron irradiation, identifying several hole traps. In irradiated samples, traps at  $H_1 = E_V + 0.42 \text{ eV}$  and  $H_2 = E_V + 0.25 \text{ eV}$  were linked to divacancy defects, while hydrogen-implanted samples revealed additional traps that may be related to divacancy-hydrogen complexes. Haesslein et al. [13], using perturbed angular correlation (PAC) spectroscopy, observed monovacancies ( $H_1 = E_V + 0.20 \text{ eV}$ ) and possible self-interstitials ( $E_1 = E_C - 0.04 \text{ eV}$ ). J. Fage-Pedersen et al. [14] examined Sb- and O-doped Ge and found vacancy-impurity complexes such as Sb-vacancy (*E*-center)  $E_1 = E_C - 0.37 \text{ eV}$ , O-vacancy (*A*-center)  $E_2 = E_C - 0.27 \text{ eV}$ , and minority-carrier trap like  $H_1 = E_V + 0.30 \text{ eV}$ , which displays a strong Poole-Frenkel effect, is Sb-related, and possibly connected to the *E*-center. C. E. Lindberg et al. [15] reported two Sb-related traps in *p*-type Ge: a single acceptor state at 0.309 eV and a donor state at 0.095 eV, both attributed to Sb-vacancy pairs. While these studies provided critical insights into point and complex defects in Ge, they primarily focused on defect identification and energy levels. However, the influence of these defects on the key transport properties, such as carrier lifetime and mobility parameters, has not been examined. Such investigations are crucial as these properties are vital for detector performance. This present study seeks to address that gap by investigating the effect of electrically active defects on the transport behavior in HPGe.

This study focuses on evaluating the activation energies and electrical behavior of intrinsic and impurity-related defects in HPGe crystals and their influence on charge transport properties. Defect-related energy levels within the bandgap can act as trapping or recombination centers, which significantly affect the performance of HPGe detectors. To investigate these effects, a combination of microwave-detected photoconductivity (MDP) carrier lifetime mapping, etch pit density (EPD) analysis, temperature-dependent Hall (TDH) measurements, and deep-level transient spectroscopy (DLTS) is employed. Together, these complementary techniques allow for a comprehensive correlation between structural and electronic defect characteristics and the transport behavior of charge carriers, including mobility and lifetime. This multi-method approach facilitates a deeper understanding of how both extended defects (e.g., dislocations) and point defects (e.g., deep acceptor or donor states) impact the electrical quality of detector-grade Ge, addressing critical knowledge gaps in the development of next-generation HPGe radiation detectors.

## 2. Methods

HPGe single crystals of 3-in. diameter were grown using the Czochralski method under a hydrogen atmosphere. The initial material for the growth has been purified up to 13 N purity using the multiple zone refining technique. The crystals were grown along the [100] direction, and the Cz process is explained elsewhere in detail. [16] Specific samples and wafers were prepared from the grown crystals for various characterizations to study the deep level defects, such as residual impurities and lattice irregularities, such as point defects (vacancies) and line defects, dislocations acting as recombination centers affecting the

carrier lifetime and mobility. In this study, the wafers and samples showing specific features of interest, particularly the ring-like structures, from various HPGe crystals, cut parallel to the (100) plane, at different sections, were investigated. The samples taken from the crystal cone are denoted as section A (top part of the crystal), the samples taken from just after the shoulder are denoted as section B (middle part of the crystal), and the samples taken from the bottom part of the crystal cylinder are designated as section C. The Hall effect and TDH measurements were performed on square samples (of size  $7 \times 7 \times 1 \text{ mm}^3$ ), while EPD and MPD measurements were performed on circular wafers with 1 mm thickness. The square samples and wafers were taken close to each other from three sections in the axial positions (A, B, C) of various crystals, and are respectively denoted as follows: sample-1 and wafer-1 from crystal-1, section C; sample-2 and wafer-2 from crystal-2, section C; sample-3 and wafer-3 along with sample-4 and wafer-4 from crystal-3, sections A and B; sample-5 and wafer-5 from crystal-4, section B. The circular wafers were chemo-mechanically polished to minimize surface and subsurface damage, ensuring reliable charge carrier lifetime measurements.

Minority carrier lifetime is an essential material property for the successful operation of HPGe radiation detectors with high efficiency. A microwave detected photoconductivity (MDP), from Freiberg Instruments, was used to map carrier lifetime in HPGe wafers. This contactless technique offers high sensitivity, spatial resolution, and fast measurement. The measurement is based on changes in microwave reflectivity caused by laser-induced excess carriers. [17] The decay of the photoconductivity signal was analyzed to extract effective carrier lifetimes via linear regression. [18] The complete details of the technique are explained elsewhere. [19–21] The measurements were performed at both RT and at 83 K. To reach such a low temperature during the measurements, the MDP equipment is constructed with a closed-cycle helium cryostat (CTI-Cryogenic). Carrier excitation is performed by a near-infrared laser diode at 980 nm with a photon energy slightly exceeding the bandgap of Ge. To ensure full carrier saturation, each measurement point was illuminated for 500 μs. The subsequent exponential decay of the photovoltage was recorded over an identical duration of 500 μs. At each scan location, the carrier lifetime was determined by averaging 10 independent measurements to enhance reliability and reduce noise. The laser was focused to a spot size of 0.5 mm, and wafer mapping was conducted with a spatial resolution of 0.5 mm. These measurement parameters were selected based on prior measurements on Ge that provided the most consistent and accurate lifetime values.

To evaluate the defect density and structural uniformity of the crystals, an etching analysis and etch pit density (EPD) estimation were performed. The complete details of the etching process are described elsewhere. [22,23] The etched wafers were then investigated using differential interference contrast microscopy. The etch-pit distribution may be non-uniform; therefore, no procedure is prescribed for selecting the regions to be counted. However, the dislocations have been counted at three different  $1 \text{ mm} \times 1 \text{ mm}$  areas located at the center, edge (R), and region between the center and edge (R/2). The EPD values were determined by counting the number of large faceted etch pits originating from the dislocation cores and divided by the investigated area.

Hall effect measurements were performed at 77 K using the Van der Pauw geometry on square Ge samples ( $7 \times 7 \times 1 \text{ mm}^3$ ) to determine carrier concentration, mobility, and resistivity. Prior to measurement, the samples were etched using an HF:  $\text{HNO}_3$  mixture and dried with nitrogen gas. Ohmic contacts were made at each corner of the sample using indium-gallium (In:Ga) eutectic to ensure reliable electrical contact. To understand the temperature dependence of carrier concentration and mobility, and to identify impurity activation energies and scattering mechanisms in HPGe, TDH measurements were performed. The measurements were carried out over a temperature range of 20 K to 300 K using a Lake Shore 7604 Hall effect measurement system, which includes a closed-cycle refrigerator cryostat and an oven module. For

TDH, ohmic contacts were formed by capacitor discharge over an Au wire using Ga:Au and Sb:Au in the contact region for *p*-type and *n*-type samples, respectively.

Deep-Level Transient Spectroscopy (DLTS) is a powerful technique for characterizing deep-level defects in semiconductors. It measures the transient capacitance response of a device, such as a Schottky diode, following a voltage pulse. DLTS investigations were carried out on Schottky diodes as test structures. The Schottky contacts on *n*-type Ge sample ( $10 \times 10 \times 1 \text{ mm}^3$  square sample) were fabricated by electron beam evaporation of platinum (Pt) in vacuum at a pressure of few  $10^{-6}$  mbar through a  $9 \text{ mm} \times 9 \text{ mm}$  square shadow mask. Ohmic contacts were fabricated by evaporation of titanium (Ti) – gold (Au) through a  $9 \times 9 \text{ mm}$  square shadow mask on the sample's back side and additionally using silver glue. The measurements were conducted using a commercial Bio-Rad DL 8000 system over a temperature range of 20–300 K. The measurement conditions included rate windows corresponding to a peak maximum emission rate of  $e_{n,\max}$  of 1.14, 11.4, and  $114 \text{ s}^{-1}$ , a reverse bias voltage  $V_r = -2 \text{ V}$ , a pulse voltage  $V_p = 0 \text{ V}$ , and a pulse width of  $t_p = 100 \mu\text{s}$ .

### 3. Measurements and results

#### 3.1. Minority carrier lifetime

Carrier lifetime mapping was performed on various HPGe crystals at RT, and some crystals revealed distinct ring-like patterns across different sections of the wafers. For two *p*-type crystals (denoted as wafer-1 and wafer-2), ring structures were observed at the core near the bottom of the crystal ingot, while a prominent ring structure appeared at the middle section of the *n*-type crystal (denoted as wafer-4), as shown in Fig. 1.

To better understand these patterns and their behavior at low temperatures (as HPGe detectors are used at liquid nitrogen (LN) temperature, 77 K), carrier lifetime mapping was extended to low temperatures. As the measurement instrument could reach only up to 83 K, all the measurements were performed at 83 K, which is not much deviated from LN temperature. These measurements aimed to study the influence of deep-level defects such as residual impurities, vacancies, and dislocations that act as recombination centers and impact both carrier lifetime and mobility. In addition, wafers exhibiting high carrier lifetime at RT (from both *n*-type and *p*-type crystals), denoted as wafer-3 and wafer-5, were selected for detailed low-temperature analysis. Details of these wafers are provided in section 2. The carrier lifetime mapped using the MPD technique at both RT and 83 K is shown in Fig. 1. To the best of the authors' knowledge, this is the first report on the full-wafer mapping of carrier lifetime at 83 K on HPGe. The average carrier lifetime values of the wafers were summarized in Table 1. For wafer-1 (Fig. 1), the RT mapping exhibits a ring structure at the center of the wafer with an average carrier lifetime of around 50  $\mu\text{s}$ , while the remaining area up to the edge shows an increased carrier lifetime of about 90  $\mu\text{s}$ , resulting in an overall average carrier lifetime of approximately 73  $\mu\text{s}$ . At 83 K, the carrier lifetime reduces by a factor of four, with an average of 16  $\mu\text{s}$ . The carrier lifetime mapping at 83 K reveals a central core structure with a lifetime of 20  $\mu\text{s}$ , an outer ring near the edge shows carrier lifetime around 15  $\mu\text{s}$ , and four small petal-like structures between the core and edge show a lifetime around 30  $\mu\text{s}$ , while the edge of the wafer shows a lifetime below 10  $\mu\text{s}$ .

Wafer-2 (Fig. 1), displayed similar ring structures at both RT and 83 K. The central ring had a lifetime of 60  $\mu\text{s}$  at RT, and the surrounding areas, till the edge of the wafers, show a lifetime of about 80  $\mu\text{s}$ , resulting in an overall average of 77  $\mu\text{s}$ . At 83 K, the average lifetime dropped to 17  $\mu\text{s}$ ; the carrier lifetimes mapping also shows a ring structure at the center of the wafer around 25  $\mu\text{s}$  and edge values below 10  $\mu\text{s}$ , mirroring the threefold reduction seen in wafer-1. Wafer-3 (Fig. 1) exhibited homogeneous carrier lifetime mapping, with an average of 109  $\mu\text{s}$  at RT and 47  $\mu\text{s}$  at 83 K, indicating a reduction in carrier lifetime by half

compared to RT lifetime. In contrast, the wafer-4 (Fig. 1) showed larger ring structures with a non-homogeneous distribution of lifetime. At RT, the ring structures at the center of the wafers show a lifetime of 30  $\mu\text{s}$ , increasing to 60  $\mu\text{s}$  outside the first ring, and reaching 100  $\mu\text{s}$  at the edge of the wafer, resulting in an average lifetime of 66  $\mu\text{s}$ . At 83 K, a similar large ring structure appeared with lifetimes around 25  $\mu\text{s}$  at the center of the wafer; the lifetime is increasing to 45  $\mu\text{s}$  toward the edge, with an overall average of 36  $\mu\text{s}$ . Wafer-5 (Fig. 1) shows a very homogeneous distribution of carrier lifetime throughout the wafer at RT. The overall average carrier lifetime obtained at RT is 153  $\mu\text{s}$ , which is the highest carrier lifetime value obtained compared to other crystals at RT. At 83 K, the carrier lifetime mapping exhibits a square-like structure (exhibiting the [100] crystallographic orientation of the surface) with a non-homogeneous distribution. The carrier lifetime at the center of the wafer with a square shape shows a non-uniform distribution ranging between 30 and 40  $\mu\text{s}$ , whereas outside the square structure, the carrier lifetime dropped to around 15 to 20  $\mu\text{s}$ . Few areas of the wafer's edges show a lifetime of almost zero microseconds. The average carrier lifetime of overall mapping is approximately 24  $\mu\text{s}$ .

#### 3.2. Dislocation densities

To understand the ring structure observed in lifetime mapping, the dislocation densities of the wafers were evaluated using a wet-chemical etching process and subsequent EPD analysis, as dislocation cores serve as preferential etching sites. After chemical etching, the wafers were examined under optical microscopy with differential interference contrast (DIC). By mapping the etch pits on the whole wafer, similar ring structures were observed (Fig. 1, right). EPD values were estimated by counting the significantly large, faceted etch pits associated with dislocation cores and then normalizing to the examined area, as presented in Fig. 2. Wafer-1 exhibits a non-uniform dislocation distribution with symmetrical characteristics along the [100] direction. The EPD value is  $1.5 \times 10^4 \text{ cm}^{-2}$  which is higher at the center of the wafer, decreases ( $8 \times 10^3 \text{ cm}^{-2}$ ) toward the mid-radius ( $R/2$ ) and increases again at the edge ( $R$ ) showing an EPD value around  $2.5 \times 10^4 \text{ cm}^{-2}$ , along the [100] direction, indicating a symmetrical variation in dislocation density across the wafer. Wafer-2 shows a non-uniform dislocation distribution with a W-shaped EPD profile. Measurements along the [100] and [110] directions reveal U-shaped distributions on each half of the wafer, resulting in an overall W-shaped pattern. Such patterns may arise due to common growth dynamics or thermal gradients during solidification, and are typical for the Czochralski-grown crystals. [24,25] Wafer-3 could not be reliably analyzed for dislocation density, as the etch pits were extremely small and not detectable, suggesting a very low dislocation density. Wafer-4 shows up to one order of magnitude lower EPD values compared to other wafers, with values increasing steadily from the center to the edge, low EPD at the center ( $1.4 \times 10^3 \text{ cm}^{-2}$ ), moderate at  $R/2$  ( $2.2 \times 10^3 \text{ cm}^{-2}$ ), and higher at the edge ( $4.4 \times 10^3 \text{ cm}^{-2}$ ). This radial variation indicates a different internal stress profile compared to that of the wafers with W-shaped EPD profiles. Wafer-5 reveals a W-shaped dislocation distribution, with high EPD at the center of the wafer of around  $1.7 \times 10^4 \text{ cm}^{-2}$ , a decrease in EPD at  $R/2$  to a value around  $7.7 \times 10^3 \text{ cm}^{-2}$ , and the highest dislocation density at the edge around  $6.7 \times 10^4 \text{ cm}^{-2}$ . The edge EPD is notably higher than in the other wafers, possibly pointing to severe thermal stress near the crystal periphery during growth. The optical micrograph (DIC) of the etched (100) wafers chosen from various sections of the HPGe crystals grown in the [100] direction is shown in Fig. 1.

#### 3.3. Impurity analyses in the crystals

The net charge carrier concentration, mobility, and resistivity of the samples selected from the center of the above described wafers 1–5, were measured by the Hall effect at 77 K (liquid nitrogen temperature). The results are summarized in Table 2. Sample-1 shows a *p*-type

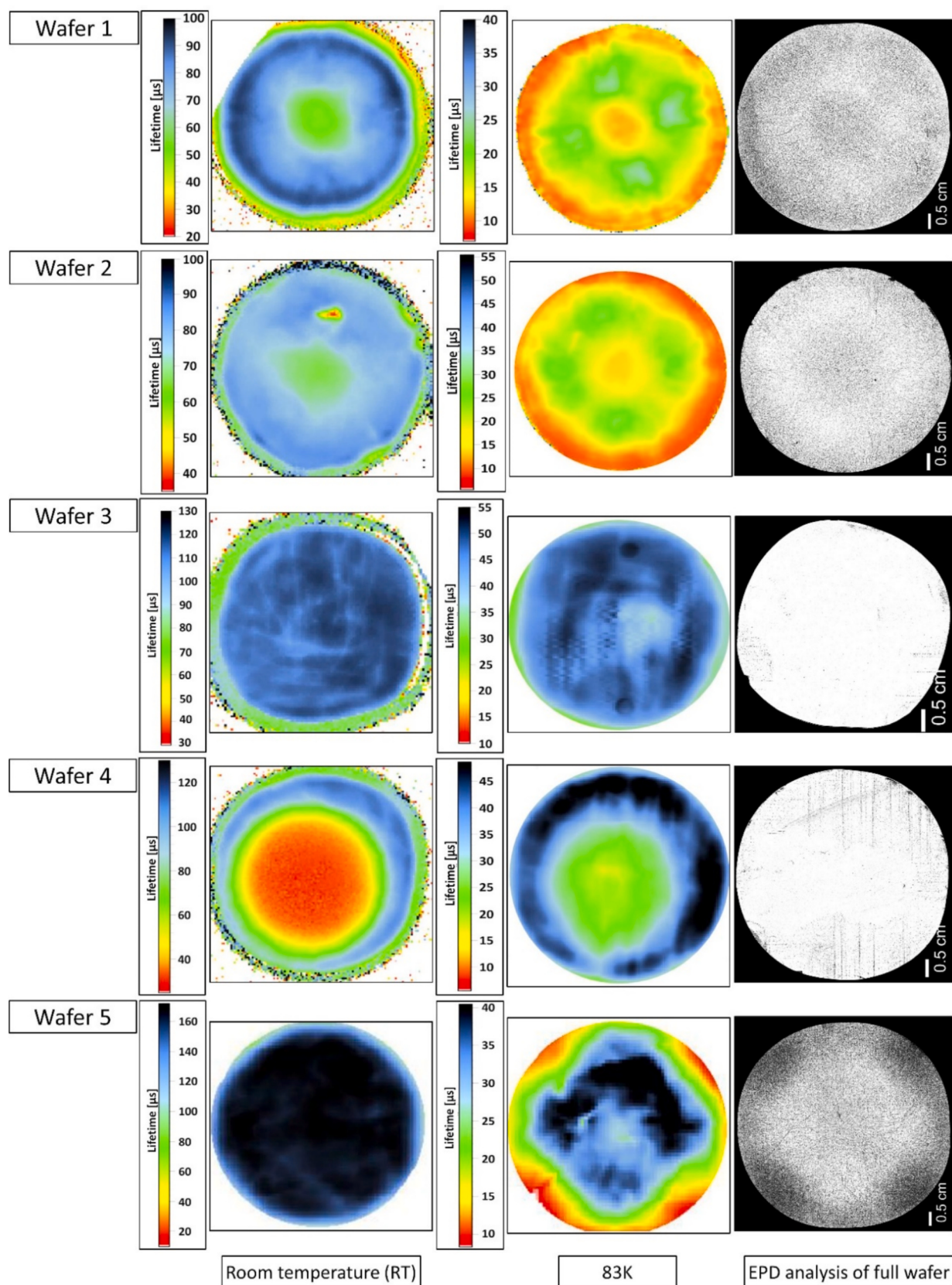


**Fig. 1.** Carrier lifetime mapping of HPGe wafers from various crystals performed at room temperature (left) and at 83 K (middle) using microwave detected photoconductivity (MDP) technique. The distribution of dislocation densities using etch pit density analysis of the same wafer (at RT) is shown in the right picture, correlating with carrier lifetime measurements.

**Table 1**

The average carrier lifetime values obtained at room temperature (RT) and 83 K.

Wafer	Crystal	Sections of the crystal	Lifetime at RT	Lifetime at 83 K [μs]
1	1	C	73	16
2	2	C	77	17
3	3	A	109	47
4	3	B	66	36
5	4	B	153	24

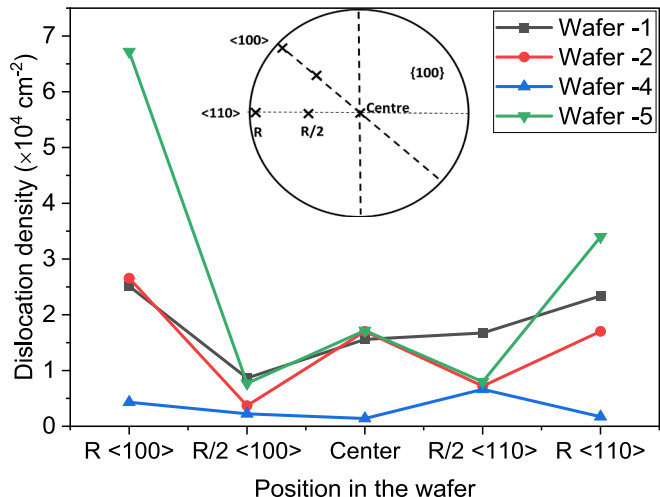


**Fig. 2.** The EPD values of various  $<100>$  HPGe crystals grown by the Cz method in  $\text{H}_2$  atmosphere. The investigated wafers are chosen from various sections of the crystals.

conductivity with net carrier concentration around  $6.3 \times 10^{12} \text{ cm}^{-3}$ , showing relatively low mobility and resistivity. Sample-2 shows a *p*-type conductivity with very high resistivity  $2.3 \times 10^8 \Omega\cdot\text{cm}$ , which indicates compensation between donors and acceptors. This compensation effect in this particular sample has been studied in detail and reported elsewhere. [26] Sample-3, and -4 show *n*-type conductivity with a carrier concentration in the range of  $2.2\text{--}4.0 \times 10^{11} \text{ cm}^{-3}$ , the mobility values are between  $3.4$  and  $2.9 \times 10^4 \text{ cm}^2 \text{ V}^{-1} \cdot \text{s}^{-1}$ , and the resistivity is around  $1.4 \times 10^3 \Omega\cdot\text{cm}$  and  $6.7 \times 10^2 \Omega\cdot\text{cm}$ , respectively. Sample-5 shows *p*-type conductivity with a carrier density of  $2.5 \times 10^{11} \text{ cm}^{-3}$ , a mobility of  $3.2 \times 10^4 \text{ cm}^2 \text{ V}^{-1} \cdot \text{s}^{-1}$ , and a resistivity value of  $1.1 \times 10^3 \Omega\cdot\text{cm}$ .

#### 3.4. Temperature-dependent Hall measurements

In order to identify the presence of deep-level impurities/defects in the samples, detailed TDH measurements were carried out in the temperature range of 20–320 K. This also facilitates to investigate the electrical properties such as carrier concentration, resistivity, and mobility with temperature. The same samples taken for Hall measurements were used for the TDH measurements as well. Sample descriptions and the details of sample preparation are provided in Section 2. Distinct *p*-type and *n*-type behavior of the respective samples could be seen from

the Hall coefficient ( $R_H$ ) vs temperature plot in Fig. 3a. In the extrinsic region (20–240 K),  $R_H$  is positive for *p*-type and negative for *n*-type samples, indicating the majority carriers are holes for *p*-type, and electrons for *n*-type. A nearly constant Hall coefficient with temperature indicates that no further ionization occurs, despite increasing thermal energy. In the intrinsic region, the thermal energy becomes high enough to excite a significant number of electrons from the valence band to the conduction band, resulting in *n*-type conductivity in Ge. For the *p*-type samples (Samples-2 and -4, with carrier concentrations  $\leq 2 \times 10^{11} \text{ cm}^{-3}$  at 77 K), the Hall coefficient ( $R_H$ ) decreases sharply with temperature and approaches near zero around 240 K, indicating the onset of mixed conductivity as intrinsic carriers become thermally excited. [27,28] For Sample 1, which has a slightly higher acceptor concentration ( $\approx 1 \times 10^{12} \text{ cm}^{-3}$  at 77 K),  $R_H$  exhibits a clear sign reversal around 285 K. This is a characteristic behavior of HPGe, where thermally generated electrons, with much higher mobility than holes, progressively dominate the total conduction, leading to an apparent *n*-type response in the intrinsic region. [27] An inset in Fig. 3(a) presents the low- $R_H$  region on an expanded y-scale, clearly highlighting the reduction and sign-reversal behavior near 240–285 K.

In carrier concentration vs inverse temperature plot (Fig. 3b), Sample-1 exhibits three step-like decreases in carrier concentration from  $6 \times 10^{12} \text{ cm}^{-3}$  to  $1 \times 10^{12} \text{ cm}^{-3}$  across temperature ranges of 250–160 K, 100–60 K, and 40–20 K. These correlate with increases in resistivity (Fig. 3c), indicating the presence of three deep-level acceptor states. Correspondingly, the hole mobility ( $\mu_p$ ) increases with decreasing temperature in the extrinsic region (Fig. 3d), reaching a very high value of  $42,000 \text{ cm}^2 \text{ V}^{-1} \cdot \text{s}^{-1}$  at 77 K. Above 200 K, the transport behavior reflects the onset of intrinsic conduction, where both electrons and holes contribute to the overall conductivity. In this temperature range, mixed-carrier effects begin to dominate, leading to apparent changes in the measured Hall coefficient and mobility that do not represent a single-carrier transport properties. Sample-2 shows a very high resistivity of  $10^8 \Omega\cdot\text{cm}$  at 90 K. As the temperature decreases there was a rapid rise in resistivity in the extrinsic region. At 100 K, the carrier concentration (Fig. 3b) is very low in the order of  $10^6 \text{ cm}^{-3}$ . As the temperature rises above 100 K, the carrier concentration increases rapidly. The mobility obtained at 100 K is about  $21,000 \text{ cm}^2 \text{ V}^{-1} \cdot \text{s}^{-1}$ . Below 80 K, Hall measurements could not be performed for sample-2 due to the resistivity exceeding  $10^9 \Omega\cdot\text{cm}$ , which exceeds the measurement limits of our setup. Sample-5 is found to maintain a nearly constant carrier concentration of  $2 \times 10^{11} \text{ cm}^{-3}$  and a resistivity of  $\sim 10^3 \Omega\cdot\text{cm}$  across the extrinsic region, with high mobility of  $46,000 \text{ cm}^2 \text{ V}^{-1} \cdot \text{s}^{-1}$  at 77 K. The mobility follows a temperature dependence of approximately  $\mu \propto T^{-2.0}$  (Fig. 3d) in the temperature range between 200 and 40 K. At higher temperatures ( $>250$  K) the mobility follows nearly constant in the range of  $\sim 1000 \text{ cm}^2 \text{ V}^{-1} \cdot \text{s}^{-1}$ . Samples-3 and -4 could only be evaluated over a temperature range extending from 320 to 190 K. Below 190 K, the data became unreliable. Sample-3 shows carrier concentration around  $2 \times 10^{11} \text{ cm}^{-3}$  between 200 and 210 K (shown clearly in Fig. 3b inset), while its resistivity increases up to  $1.7 \times 10^4 \Omega\cdot\text{cm}$  at 200 K. Mobility increases up to  $4041 \text{ cm}^2 \text{ V}^{-1} \cdot \text{s}^{-1}$  at 210 K, then sharply drops to  $1500 \text{ cm}^2 \text{ V}^{-1} \cdot \text{s}^{-1}$  at 200 K. Sample-4 exhibits a stable carrier concentration of  $\sim 3 \times 10^{11} \text{ cm}^{-3}$  across the same temperature range, with resistivity ranging between 3 and  $5 \times 10^3 \Omega\cdot\text{cm}$ . Its mobility increases from 1000 to 5000

**Table 2**

Hall measurement data of various HPGe crystals at selected sections of interest for defect analyses.

Sample	Crystal	Sections of the crystal	Type	Carrier concentration [ $1/\text{cm}^3$ ]	Mobility [ $\text{cm}^2 \text{ V}^{-1} \cdot \text{s}^{-1}$ ]	Resistivity [ $\Omega\cdot\text{cm}$ ]
1	1	C	<i>p</i>	$6.3 \times 10^{12}$	$7.6 \times 10^3$	$1.4 \times 10^2$
2	2	C	<i>p</i>	—	—	$2.3 \times 10^8$ (91 K)
3	3	A	<i>n</i>	$2.2 \times 10^{11}$	$3.4 \times 10^4$	$1.4 \times 10^3$
4	3	B	<i>n</i>	$4.0 \times 10^{11}$	$2.9 \times 10^4$	$6.7 \times 10^2$
5	4	B	<i>p</i>	$2.5 \times 10^{11}$	$3.2 \times 10^4$	$1.1 \times 10^3$

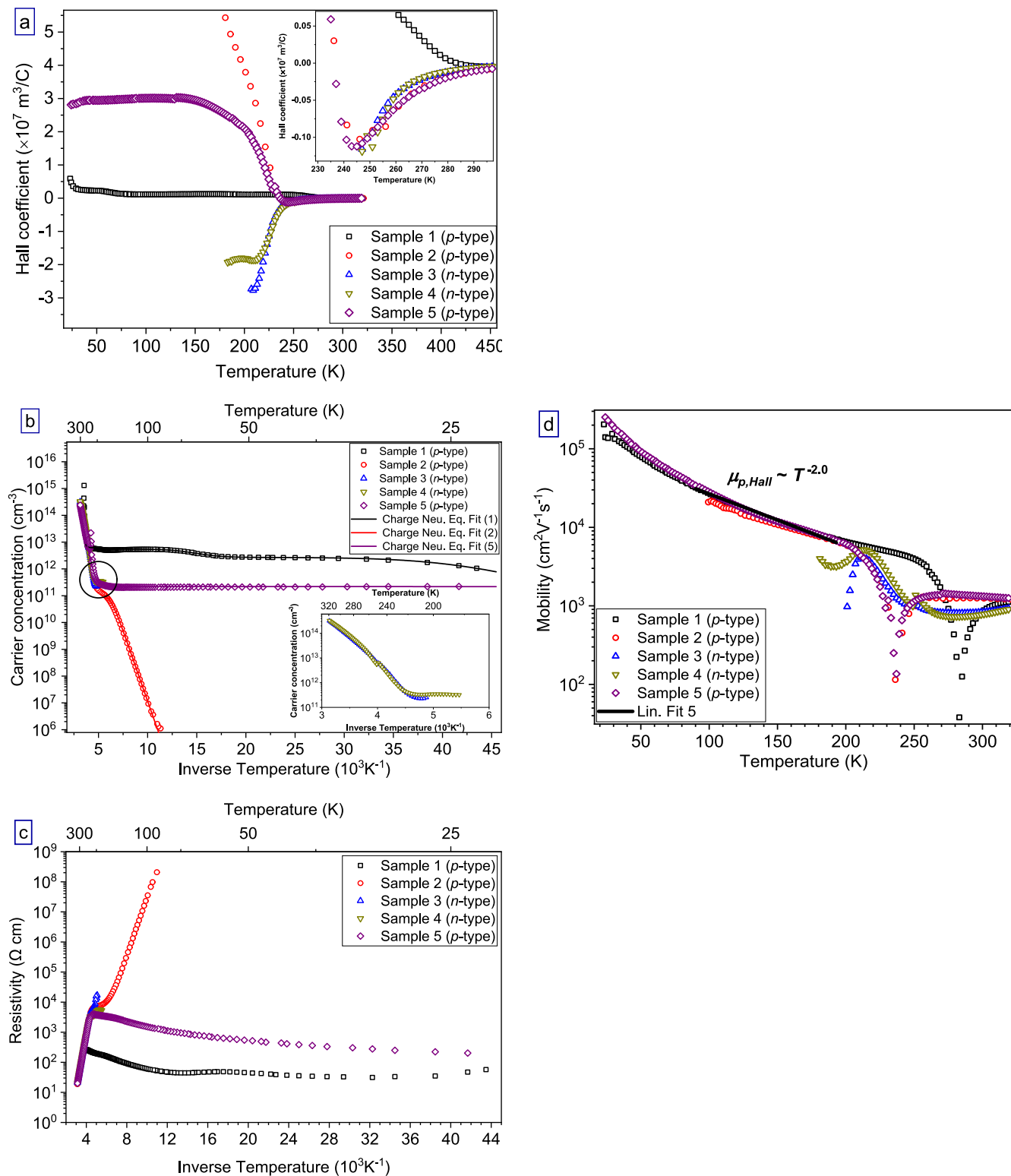


**Fig. 3.** Temperature-dependent resistivity and Hall measurement data of various HPGe crystals at different sections. The inset (referring to the circle) in the carrier concentration vs. temperature plot highlights samples-3 and -4, while the inset in the mobility vs. temperature plot shows samples-1 and -5, illustrating the transition from intrinsic to extrinsic (n-type to p-type) behavior depending on doping concentration.

$\text{cm}^2 \text{ V}^{-1} \text{ s}^{-1}$  between 250 and 215 K, before dropping to  $3000 \text{ cm}^2 \text{ V}^{-1} \text{ s}^{-1}$  at 190 K. Both samples display a slight dip and rise in mobility around 245–250 K, likely due to the transition from extrinsic to intrinsic conduction (n-type – n-type transition).

### 3.5. Deep-level transient spectroscopy measurement

In Fig. 4a, the DLTS-spectrum of sample-4 measured on a Pt Schottky contact. As can be seen, a single distinct negative peak is found between 150 K and 190 K at a peak position at 166 K for the emission rate at the peak maximum of  $114 \text{ s}^{-1}$ . The apparent activation energy derived from

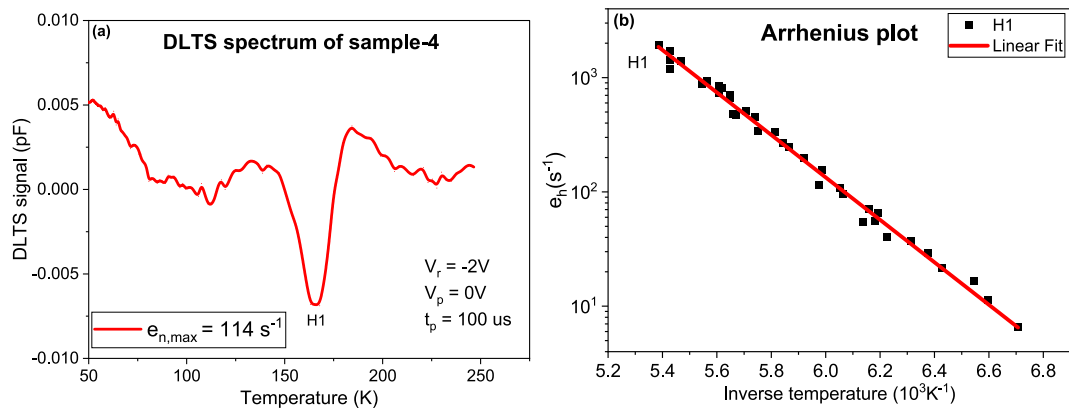


**Fig. 4.** (a) A DLTS spectrum measured for sample-4 obtained using a rate window corresponding to a peak emission rate of  $e_{n,\max} = 114\text{ s}^{-1}$ , with a reverse bias  $V_r = -2\text{ V}$ , the pulse voltage  $V_p = 0\text{ V}$ , and the pulse width  $t_p = 100\text{ }\mu\text{s}$ . (b) Arrhenius plot of the temperature-dependent hole emission rates ( $e_h$ ) for the defect level labeled H1, measured in the same sample-4. The extracted energy values represent the  $T^2$  corrected trap depths,  $E_{CT}$ .

an Arrhenius plot is 0.34 eV. The corresponding capture cross-section is found to be  $4.1 \times 10^{-14}\text{ cm}^{-2}$ . Further, a trap concentration of  $1.6 \times 10^8\text{ cm}^{-3}$  has been derived from Fig. 4b.

#### 4. Discussion

The experimental (MDP, EPD) results show that dislocations significantly affect the minority carrier lifetime of electrons and holes in Ge. Wafers-1 and -2, taken from the bottom sections of two different *p*-type HPGe crystals, exhibit distinct dislocation-related features. Lifetime mapping at 83 K reveals a petal-like structure with a central core that mirrors the dislocation distribution in the etched surfaces. Areas near the center and edges of the wafers show higher dislocation densities ( $1.5\text{--}2.6 \times 10^4\text{ cm}^{-2}$ ), where carrier lifetimes are reduced to 0–20  $\mu\text{s}$ . In contrast, regions with lower dislocation densities ( $3\text{--}8 \times 10^3\text{ cm}^{-2}$ ) exhibit increased lifetimes around 30  $\mu\text{s}$ . This correlation indicates that dislocations and dislocation-related defects, which are electrically active at 83 K, serve as recombination centers and reduce the minority carrier lifetime, as clearly observed in Fig. 1 for wafers-1 and -2. Moreover, the core regions of both wafers show lower lifetimes even at RT, suggesting that these defects are electrically active across a wide temperature range.

TDH measurements (Fig. 3b) for sample-1, extracted from the center of wafer-1, show a decrease in carrier concentration within the extrinsic region at three distinct steps. Correspondingly, the resistivity curve displays a slight increase in resistivity at three distinct steps, indicating the presence of multiple deep-level acceptors in this *p*-type crystal. [29] To estimate the individual defect concentrations and electrical activation energy in sample-1, the temperature-dependent carrier concentration data were fitted using the charge neutrality equation (Eq. 1). The number of thermally generated carriers in the conduction and valence bands were calculated using the effective density of states, which depend on the density-of-states effective masses of electrons and holes in Ge. For Ge, the effective mass of electrons is  $m_e^* = 0.56 m_0$  and of holes is  $m_h^* = 0.29 m_0$ , where  $m_0$  is the free electron mass. [30,31] These values are used to compute the effective density of states in the conduction band  $N_C$ , and the valence band  $N_V$ , which are essential for determining the carrier concentrations as a function of the Fermi level and temperature. The defect model includes four acceptor levels: one shallow acceptor concentration  $N_{A1}$  (representing the sum of fully ionized shallow acceptors) and three deep acceptors  $N_{A2}$ ,  $N_{A3}$ ,  $N_{A4}$ , corresponding to thermal ionization ranges of 20–40 K, 60–100 K, and 160–250 K, respectively. Additionally, one shallow donor concentration  $N_{D1}$ , assumed to be fully ionized and acting as a compensating defect, is also included. As shallow defects are fully ionized, only the ionization energies of the three deep acceptors  $E_{A2}$ ,  $E_{A3}$ ,  $E_{A4}$  are temperature-

dependent, and thus included in the charge neutrality equation.

$$p\left(\frac{1}{T}\right) = N_{A1}^- + \frac{N_{A2}}{1 + 2 \exp((E_{A2} - E_f(T))/k_B T)} + \frac{N_{A3}}{1 + 2 \exp((E_{A3} - E_f(T))/k_B T)} + \frac{N_{A4}}{1 + 2 \exp((E_{A4} - E_f(T))/k_B T)} - N_{D1}^+ \quad (1)$$

Where  $k_B$  represents the Boltzmann constant, and  $E_f(T)$  denotes the Fermi energy at the specified temperature. The charge carrier concentration is obtained by solving Eq. (1) with the free parameters ( $N_{A1}$ ,  $N_{A2}$ ,  $N_{A3}$ ,  $N_{A4}$ ,  $N_{D1}$ ,  $E_{A2}$ ,  $E_{A3}$ ,  $E_{A4}$ ), is summarized in Table 3. The resultant fit is illustrated as a grey line in Fig. 3b.

The carrier concentrations of various impurities and defects in the sample-1 were determined through fitting the TDH measurement data. The fitting results (Table 3) revealed a shallow acceptor concentration, assumed to arise from elements such as boron (B) and aluminium (Al), with a value of approximately  $N_{A1} \approx 2.0 \times 10^{12}\text{ cm}^{-3}$ . A shallow donor concentration, attributed to phosphorus (P), was estimated as  $N_{D1} \approx 6.3 \times 10^{12}\text{ cm}^{-3}$ . In addition to shallow levels, the fitting indicates the presence of multiple deep acceptor levels with ionization energies  $E_{A2} = 0.019\text{ eV}$ ,  $E_{A3} = 0.065\text{ eV}$ ,  $E_{A4} = 0.205\text{ eV}$  and concentrations of  $N_{A2} \approx 7.0 \times 10^{12}\text{ cm}^{-3}$ ,  $N_{A3} \approx 2.8 \times 10^{12}\text{ cm}^{-3}$ ,  $N_{A4} \approx 8.5 \times 10^{11}\text{ cm}^{-3}$ , respectively. The deep level with an activation energy of  $E_{A4} = 0.205\text{ eV}$  corresponds to a defect state that becomes electrically active in the temperature range of 160 K to 250 K, as identified from the TDH measurements. According to several studies in the literature [13,32–35], the activation energy of 0.205 eV is commonly associated with vacancy-related defects in a *p*-type Ge, which become electrically active at around 200 K. This strongly supports the interpretation that the observed deep level is likely due to lattice vacancies acting as deep acceptor states in the HPGe. The second level, observed at 0.065 eV, lies close to the 0.08 eV defect level that de-ionizing around 65 K, as reported by E. E. Haller et al., [36] in dislocation-free HPGe crystals grown in a hydrogen atmosphere. This level was attributed to the formation of divacancy-hydrogen ( $V_2\text{H}$ ) complexes, which are known to act as deep traps and degrade detector performance. Although our samples are not dislocation-free, the proximity of this level to  $E_v + 0.08\text{ eV}$  raises the possibility that hydrogen-related defects, or interactions between dislocations and hydrogen, may contribute to its formation. Furthermore, G. S. Hubbard et al. [8] reported an activation energy of  $E_H = E_v + 0.02\text{ eV}$  in HPGe crystals with dislocation densities around  $\sim 10^4\text{ cm}^{-2}$ , measured in the temperature range 30 K – 20 K. Similarly, M. Van Sande et al. [37] and E. Simeon et al. [38] reported a level at  $E_v + 0.025\text{ eV}$  in *p*-type HPGe, having grown-in dislocations. This level is commonly attributed to [112] grown-in dislocations and typically appears in DLTS

**Table 3**

Fitting data of the charge neutrality equation to the temperature dependent carrier concentration of sample-1.

	$N_{D1}$ ( $\text{cm}^{-3}$ )	$N_{A1}$ ( $\text{cm}^{-3}$ )	$N_{A2}$ ( $\text{cm}^{-3}$ )	$E_{A2}$ (eV)	$N_{A3}$ ( $\text{cm}^{-3}$ )	$E_{A3}$ (eV)	$N_{A4}$ ( $\text{cm}^{-3}$ )	$E_{A4}$ (eV)
Sample-1	$\sim 6.3 \times 10^{12}$	$\sim 2.0 \times 10^{12}$	$\sim 7 \times 10^{12}$	0.019	$\sim 2.8 \times 10^{12}$	0.065	$\sim 8.5 \times 10^{11}$	~0.205

measurements conducted around 20–30 K. The shallow level  $E_{A2} = 0.019$  eV observed in our study closely matches these reported values, suggesting that it may be associated with dislocation-related defects. Dislocations can introduce electrically active centers within the bandgap, some of which may act as traps or recombination centers depending on their energy level. While deep levels associated with dislocations can significantly impact electrical properties such as the minority carrier lifetime in HPGe. However, shallow levels (e.g., ~0.019 eV) are unlikely to serve as efficient recombination centers due to rapid thermal re-ionization. In summary, the extracted shallow and deep level concentrations, along with their respective activation energies, provide strong evidence for both impurity-induced and defect-related electrical activity in the crystal. The shallow impurities are primarily responsible for the electrical conductivity by donating free carriers, while the deep levels, which may be associated with dislocations and vacancy-type defects, can act as traps or recombination centers, affecting carrier lifetime at 83 K. These findings align well with known defect behaviours in HPGe and its carrier lifetime measurements.

The TDH measurement result for sample-2, taken from the center of wafer-2 is previously reported by our group in detail [26]. In the extrinsic temperature region, the carrier concentration decreases by almost four orders of magnitude, while the resistivity increases by the same order of magnitude. The decrease in the carrier concentration and increase in the resistivity in the extrinsic region with an activation energy of 0.195 eV indicates a deep level defect. TDH data for this sample could be reliably measured down to 90 K. Below this temperature, the measurements became unstable due to the very high sample resistance, which makes difficult to measure the Hall data. This increase in resistance most likely originates either from an increase in contact resistance or from the sample itself, where the deep-level defect is thermally activated and strongly influences the electrical characteristics. [39,40] Nickel (Ni) impurities in Ge are known to introduce deep acceptor levels at  $E_v + 0.22$  eV and as well at  $E_c 0.30$  eV. [41] Additionally, vacancy-related defects with activation energies of 0.19 and 0.21 eV have also been reported in the literature. [33,34,42] Therefore, the observed deep level in sample-2 can be attributed either to residual Ni contamination or to divacancy-related defects. These deep acceptor states act as carrier traps of donors, leading to a strong compensation and a significant reduction in free carrier concentration (Fig. 4b). [43] This defect level is very close to the one observed in sample-1 (0.205 eV), which suggests that the core region of the HPGe crystals contains vacancy-related defects. These defects remain electrically active at both RT and 83 K, where they act as recombination centers, thereby reducing the carrier lifetime. In sample-2, the degree of compensation is noticeably higher than in sample-1. This indicates that the concentration of the deep-level acceptor in sample-2 is relatively larger, and that this defect dominates the charge-balance dynamics in the core region of the crystal. To quantify the concentrations of impurities, the temperature-dependent carrier concentration data were fitted using the charge neutrality equation (Eq. 2). The model assumes one shallow acceptor concentration  $N_{A1}$  (representing all shallow acceptors, which are fully ionized above 90 K), one deep acceptor concentration  $N_{A2}$  (explaining the thermal ionization between 90 K and 200 K), and one shallow donor concentration  $N_{D1}$ . Due to full ionization of the shallow defects, only the ionization of the deep acceptor  $E_{A2}$  contributes to the temperature dependence:

$$P\left(\frac{1}{T}\right) = N_{A1}^- + \frac{N_{A2}}{1 + 2 \exp((E_{A2} - E_f(T)) / k_B T)} - N_{D1}^+ \quad (2)$$

**Table 4**

Fitting data of the charge neutrality equation to the temperature dependent carrier concentration of sample-2.

	$N_{D1}$ ( $\text{cm}^{-3}$ )	$N_{A1}$ ( $\text{cm}^{-3}$ )	$N_{A2}$ ( $\text{cm}^{-3}$ )	$E_{A2}$ (meV)
Sample-2	$\sim 7.0 \times 10^{11}$	$\sim 7.0 \times 10^{10}$	$\sim 7.6 \times 10^{11}$	195

The extracted fitting parameters are summarized in Table 4, and the corresponding fit is shown as the red line in Fig. 3b. (See Table 5.)

The mobility of sample-2 shows a deviation from the expected  $T^{-2.0}$  dependence. This decrease in mobility is also associated with such strong compensation due to deep defects, resulting in enhanced impurity/defect scattering as well as neutral impurity scattering. [44,45] The mobility of sample C at 100 K is about  $21,000 \text{ cm}^2 \text{ V}^{-1} \cdot \text{s}$ , while the carrier concentration is approximately  $10^7 \text{ cm}^{-3}$ .

Carrier lifetime mapping of wafer-5, taken from the middle region of p-type HPGe crystal, reveals a higher lifetime at RT, approximately 153  $\mu\text{s}$ , compared to other wafers. However, at 83 K, the carrier lifetime mapping exhibits a distinct square-shaped pattern that corresponds directly with the EPD mapping. The EPD mapping shows this square region has a lower dislocation density in the range of  $8 \times 10^3$ – $1.7 \times 10^4 \text{ cm}^{-2}$ , while the surrounding area displays higher dislocation densities between  $3 \times 10^4$ – $6 \times 10^4 \text{ cm}^{-2}$ . This dislocation density distribution is mirrored in the low-temperature carrier lifetime data: within the square region, the lifetime ranges from 30 to 40  $\mu\text{s}$ , whereas in the high dislocation density zones, it drops significantly to 10 to 15  $\mu\text{s}$  at 83 K. TDH measurements across the extrinsic region confirm a uniform carrier concentration and resistivity, indicating the absence of deep-level impurities. Additionally, carrier mobility increases with decreasing temperature, reaching a highest value of approximately  $4.6 \times 10^4 \text{ cm}^2 \text{ V}^{-1} \cdot \text{s}^{-1}$  at 77 K. Hence, to evaluate the impurity-related carrier concentrations in Sample-5, the TDH data were fitted using a charge neutrality equation (Eq. 3).

$$P\left(\frac{1}{T}\right) = N_{A1}^- + \frac{N_{A2}}{1 + 2 \exp((E_{A2} - E_f(T)) / k_B T)} - N_{D1}^+ \quad (3)$$

This model accounts for the contributions of both shallow and deep impurity states. Specifically, it incorporates one shallow acceptor level  $N_{A1}$  representing the combined effect of fully ionized acceptors likely introduced by elements such as B and Al. A single shallow donor concentration  $N_{D1}$ , attributed to P, was also included as a compensating donor and assumed to be fully ionized across the studied temperature range. In addition to these shallow states, the model integrates a deep acceptor level  $N_{A2}$ , with a thermally activated ionization energy of approximately 0.25 eV. This deep level becomes electrically active between 160 K and 250 K, contributing to the carrier dynamics in this range. The carrier concentration of shallow level impurities and deep level defect is obtained from the fitting is given in following Table 5.

Furthermore, the fitting indicated the presence of at least one deep acceptor level with an ionization energy 0.25 eV and a concentration of  $1 \times 10^{11} \text{ cm}^{-3}$ . Various studies [9,11,12] on irradiation-induced defects in Ge studied by DLTS, reveal a hole trap  $E_H = E_v + 0.25$  eV in the

**Table 5**

Fitting data of the charge neutrality equation to the temperature dependent carrier concentration of sample-5.

	$N_{D1}$ ( $\text{cm}^{-3}$ )	$N_{A1}$ ( $\text{cm}^{-3}$ )	$N_{A2}$ ( $\text{cm}^{-3}$ )	$E_{A2}$ (eV)
Sample-5	$\sim 7.8 \times 10^{11}$	$\sim 1.0 \times 10^{12}$	$\sim 1 \times 10^{11}$	0.25

temperature range of 160 to 230 K. This defect level can be ascribed to vacancy-related defects. The obtained concentration of deep-level defect  $N_{A2}$  is one order of magnitude less than the shallow-level acceptor concentration. However, due to its location within the bandgap and possible proximity to dislocations, it may still play a role in hole trapping. In wafer-5 if dislocations distributed throughout the wafer are assumed to be the dominant recombination centers affecting carrier lifetime at 83 K (while having a negligible impact on mobility), and each dislocation acts as a non-radiative recombination center, the recombination rate ( $\lambda$ ) can be described by:

$$\lambda = \frac{\Delta p}{\tau} = \sigma_R \cdot N_D \cdot \Delta p \quad (4)$$

where,

- $\Delta p$  is the excess minority carrier concentration,
- $N_D$  is the dislocation density,
- $\tau$  is the carrier lifetime,
- $\sigma_R$  is the recombination capture coefficient (cm/s).

Using the measured lifetime values at 83 K and known excess carrier concentration of  $2 \times 10^{11} \text{ cm}^{-3}$  at around 83 K, extracted from TDH measurements, the recombination rate was calculated at different dislocation densities (assuming that the recombination is mainly due to dislocations). These results are summarized in Fig. 5, which shows a clear trend of increasing recombination rate with increasing dislocation density. This behavior confirms that the dislocations in the wafer are electrically active, especially at low temperatures, acting as efficient recombination centers and significantly degrading the carrier lifetime. The mobility, however, remains unaffected, reinforcing the conclusion that dislocations are mainly responsible for reducing the carrier lifetime in these samples than the residual impurities.

Wafers-3 and -4 were taken out from the same crystal (*n*-type), with wafer-3 taken near the top and wafer-4 from the middle section of the crystal. Carrier lifetime mapping of wafer-3 (Fig. 1) revealed spatially uniform lifetimes ranging between 110 and 130  $\mu\text{s}$  at RT and 40 and 55  $\mu\text{s}$  at 83 K. This reduced carrier lifetime by half of the value from RT to 83 K shows that the activation of recombination centers is more prominent at lower temperatures. The etch pits revealed in the EPD analysis are very small and could not be counted, and hence the dislocation density is assumed to be lower than  $10^3 \text{ cm}^{-2}$ . TDH measurements revealed a resistivity increase to approximately  $1.7 \times 10^4 \Omega\text{-cm}$  within the extrinsic conduction regime (220–200 K). Below 200 K, the data became unreliable. This anomaly indicates the presence of electrically

active deep-level defects that act as compensating centers. The carrier mobility increases while decreasing the temperature up to 210 K as expected, due to reduced phonon scattering. However, it then drops sharply around 200 K, indicating the increased impurity or defect scattering. These phenomena are attributed to vacancy-related deep-level defects, commonly known to introduce compensating acceptor levels in *n*-type Ge. These defects can severely impact mobility and resistivity by fully compensating the material and complicating accurate electrical measurements. Despite this, lifetime mapping at 83 K remained spatially uniform, indicating that these deep-level defects are evenly distributed across the wafer. In contrast, lifetime mapping of wafer-4 exhibited a pronounced ring-like structure both at RT and at 83 K, signifying non-uniform defect distribution. This spatial pattern directly mirrored the dislocation distribution observed in the EPD mapping, where dislocation density was lower at the wafer center but increased radially toward the edges. TDH measurements on sample-4 showed an increase in carrier concentration and a decrease in resistivity with increasing temperature in the range of 180–250 K. However, reliable Hall carrier concentration data were obtained only between approximately 300 K and 200 K, which lies close to the intrinsic conduction regime, where the extraction of electron concentration is not accurate. Below 200 K, the Hall coefficient exhibited strong fluctuations and did not follow a consistent trend, preventing meaningful carrier concentration estimation. Since the activation energy of the deep-level defect can only be determined from the extrinsic characteristics (i.e., below 200 K), the available Hall data range was insufficient for a reliable fit. Therefore, the activation energy of the deep-level defect in Sample-4 was determined from the DLTS measurements, where the defect state is clearly resolved. The mobility in Sample-4 increases from 250 K to 220 K, shows a slight dip at 190 K, and then recovers. This dip is attributed to thermal activation of a deep-level acceptor, which begins to trap free carriers in this temperature range. The activation of this defect increases the number of ionized scattering centers, which temporarily reduces the mobility. However, a measurement artifact cannot be completely excluded, since the Hall signal becomes weaker in this temperature range. DLTS analysis of sample-4 (Fig. 4a) revealed a negative peak between 150 and 190 K, corresponding to a deep-level defect with an activation energy of approximately 0.34 eV and a defect concentration of  $1 \times 10^8 \text{ cm}^{-3}$ . The negative signal polarity in DLTS indicates a minority carrier trap, i.e., a hole trap in *n*-type material, which may be a characteristic of an acceptor like deep states. The observed defect level at 0.34 eV is identified as vacancy-related centers in *n*-type Ge, and similar activation energies are reported in the literature. [14,15,35,46,47] Specifically, these levels have been associated with vacancy-donor complexes such as *E*-centers (a phosphorus-vacancy complex), known to form in Ge doped with group-V elements. Group-V impurities like phosphorus have a strong affinity for vacancies and readily form electrically active complexes that behave as deep acceptors, especially in dislocation-free regions where vacancy diffusion is less constrained. The combined analysis of MDP, EPD mapping, TDH, and DLTS measurements on wafers-3 and -4 provides compelling evidence that the dominant electrically active defects in these *n*-type HPGe crystals are vacancy-related deep acceptors, most likely *E*-centers, which significantly influence carrier lifetime and mobility. In wafer-3, the uniform distribution of such defects results in spatially homogeneous electrical behavior, whereas in wafer-4, radial inhomogeneity in dislocation density directly influences defect distribution and recombination dynamics. The detection of a 0.34 eV deep level and its correlation with known vacancy-donor complexes underscores the critical role of intrinsic point defects in determining the electrical performance of HPGe-based devices.

The results reveal a strong correlation between crystal defects and charge carrier properties in HPGe crystal grown by the Czochralski method under a hydrogen atmosphere. EPD mapping showed a distinctive ring-shaped dislocation distribution, which matched the non-uniform carrier lifetime patterns observed through MDP measurements.

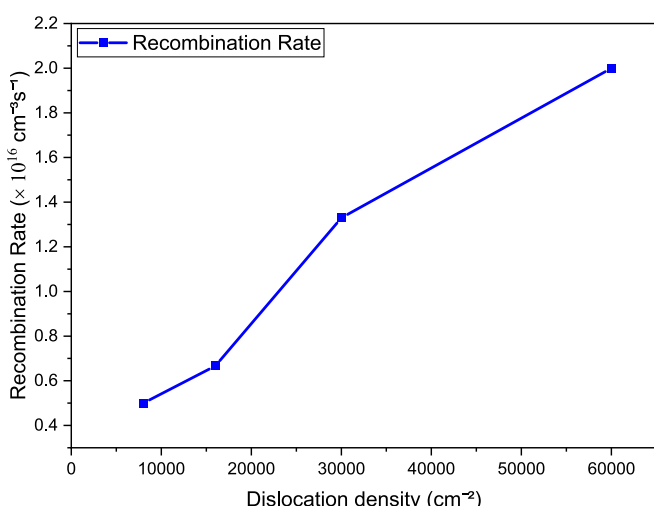


Fig. 5. Recombination Rate as a function of dislocation density at 83 K for Wafer-5.

Regions with high dislocation densities exhibited significantly lower lifetimes, confirming the impact of extended defects. Surprisingly, even areas with very low dislocation density showed reduced lifetime, suggesting the presence of electrically active point defects such as vacancies or impurity-vacancy complexes. TDH measurements further supported this, indicating several deep-level defects with activation energies of 0.019 eV, 0.065 eV, 0.2 eV, and 0.25 eV in *p*-type material. DLTS analysis of *n*-type samples identified a minority carrier trap at 0.34 eV, which may be associated with P-vacancy complexes. Overall, the findings demonstrate that both extended and point defects critically influence carrier lifetime and mobility both at RT and low temperatures.

## 5. Summary

In this study, the defect-related carrier transport properties of HPGe crystals grown by the Czochralski method under a hydrogen atmosphere were investigated, aiming for improvements in material quality for radiation detector applications. Comprehensive analyses were performed using MDP, EPD, TDH, and DLTS. Minority carrier lifetime measurements revealed non-uniform distributions with ring-shaped patterns across the wafers. These features were consistent at both RT and 83 K, though lifetime values at low temperature were significantly reduced up to threefold. EPD mapping showed that these ring structures well correlate with variations in dislocation density, which ranged from  $1 \times 10^3$  to  $2 \times 10^4 \text{ cm}^{-2}$ . Interestingly, even dislocation-free regions exhibited reduced carrier lifetimes, indicating the presence of deep-level point defects such as intrinsic vacancies or impurity-related vacancy complexes. TDH measurements on *p*-type samples with ring structures at core revealed deep-level activation energies of 0.019 eV, 0.065 eV, 0.2 eV, and 0.25 eV, associated with both vacancy- and dislocation-related defects. The highest measured Hall mobility was obtained in the *p*-type sample, and it is  $\sim 46,000 \text{ cm}^2 \text{ V}^{-1} \cdot \text{s}^{-1}$ , which is a good measure for the material quality for detectors. DLTS analysis of *n*-type samples identified a minority carrier (hole) trap with an activation energy of 0.34 eV, which may be linked to P-vacancy complexes (*E*-centers), especially prominent in low-dislocation areas. This work emphasizes the critical interplay between extended defects (dislocations) and point defects in determining the electrical behavior of HPGe. While dislocations strongly degrade the carrier lifetime, they appear to have a limited effect on carrier mobility. The point defects related to *E*-centers have a significant impact on carrier lifetime and mobility. The findings from this study underscore the need for precise control of both defect types in HPGe crystal performance for high-sensitivity radiation detectors, and the results can be taken as feedback for optimizing the crystal growth.

## CRediT authorship contribution statement

**Pradeep Chandra Palletti:** Writing – original draft, Validation, Methodology, Investigation, Formal analysis, Data curation, Conceptualization. **Uta Juda:** Writing – review & editing, Validation, Formal analysis, Data curation. **Palvan Seyidov:** Writing – review & editing, Validation, Formal analysis. **Mike Pietsch:** Formal analysis, Data curation. **Nadine Schüler:** Writing – review & editing, Validation, Formal analysis, Data curation. **Andreas Fiedler:** Writing – review & editing, Validation, Formal analysis. **R. Radhakrishnan Sumathi:** Writing – review & editing, Writing – original draft, Supervision, Resources, Project administration, Methodology, Investigation, Funding acquisition, Formal analysis, Conceptualization.

## Declaration of competing interest

The authors declare that they have no known competing financial interests or personal relationships that could have appeared to influence the work reported in this paper.

## Acknowledgement

The authors gratefully acknowledge financial support from the German Federal Ministry for Research, Technology, and Space (BMFTR) within the collaborative project LEGEND (grant numbers 05A20BC2 and 05A23BC2). We thank Dr. Iryna Buchovska for her support during the lifetime measurements at room temperature and also proof-reading the manuscript. Special thanks to Ing. Thanga Kumar (Freiberg Instruments GmbH) for providing the opportunity to perform lifetime measurements at low temperature. We also thank Dr. Martin Handweg for fruitful discussions on temperature-dependent Hall measurements. The support from Aravind Subramanian for material preparation is acknowledged. We further thank the IKZ staff for their assistance with crystal cutting and polishing, especially Thomas Wurche, Katrin Berger, and Manuela Imming-Friedland.

## Data availability

Data will be made available on request.

## References

- [1] W.L. Hansen, E.E. Haller, MRS Proc. 16 (1982) 1, <https://doi.org/10.1557/PROC-16-1>.
- [2] P.A. Tove, Sensors Actuators 5 (1984) 103–117, [https://doi.org/10.1016/0250-6874\(84\)80001-3](https://doi.org/10.1016/0250-6874(84)80001-3).
- [3] L.S. Darken, C.E. Cox, Semiconductors and Semimetals, Academic Press, 1995, pp. 23–83, [https://doi.org/10.1016/S0080-8784\(08\)62741-6](https://doi.org/10.1016/S0080-8784(08)62741-6).
- [4] Q. Looker, Fabrication Process Development for High-Purity Germanium Radiation Detectors with Amorphous Semiconductor Contacts, Ph.D. thesis, University of California, 2014. Available at, <https://escholarship.org/uc/item/1d14c7t8>. accessed December 29, 2023.
- [5] A. Owens, A. Peacock, Nucl. Instrum. Methods Phys. Res. A 531 (2004) 18–37, <https://doi.org/10.1016/j.nima.2004.05.071>.
- [6] E.E. Haller, W.L. Hansen, F.S. Goulding, Adv. Phys. 30 (1981) 93–138, <https://doi.org/10.1080/00018738100101357>.
- [7] W.L. Hansen, R.H. Pehl, E.J. Rivet, F.S. Goulding, Nucl. Inst. Methods 80 (1970) 181–186, [https://doi.org/10.1016/0029-554X\(70\)90759-7](https://doi.org/10.1016/0029-554X(70)90759-7).
- [8] G.S. Hubbard, E.E. Haller, J. Electron. Mater. 9 (1980) 51–66, <https://doi.org/10.1007/BF02655214>.
- [9] P.M. Mooney, M. Cherki, J.C. Bourgois, J. Phys. Lett. 40 (1979) L19–L22, <https://doi.org/10.1051/jphyslet:0197900400201900>.
- [10] N. Fukuoka, H. Saito, Jpn. J. Appl. Phys. 20 (1981) L519, <https://doi.org/10.1143/JJAP.20.L519>.
- [11] N. Fukuoka, H. Saito, Jpn. J. Appl. Phys. 21 (1982) 930, <https://doi.org/10.1143/JJAP.21.930>.
- [12] K. Ito, J.W. Corbett, Jpn. J. Appl. Phys. 22 (1983) L724, <https://doi.org/10.1143/JJAP.22.L724>.
- [13] H. Haesslein, R. Sielemann, C. Zistl, Phys. Rev. Lett. 80 (1998) 2626–2629, <https://doi.org/10.1103/PhysRevLett.80.2626>.
- [14] J. Fage-Pedersen, A.N. Larsen, A. Mesli, Phys. Rev. B 62 (2000) 10116–10125, <https://doi.org/10.1103/PhysRevB.62.10116>.
- [15] C.E. Lindberg, J.L. Hansen, P. Bomholt, A. Mesli, K.B. Nielsen, A.N. Larsen, L. Dobaczewski, Appl. Phys. Lett. 87 (2005) 1–3, <https://doi.org/10.1063/1.211268>.
- [16] R.R. Sumathi, A. Gybin, K.P. Gradwohl, P.C. Palletti, M. Pietsch, K. Irmscher, N. Dropka, U. Juda, Cryst. Res. Technol. 58 (2023) e202200286, <https://doi.org/10.1002/crat.202200286>.
- [17] D. Walter, P. Rosenstiel, F. Kopp, S. Reber, B. Berger, W. Warta, 25th European Photovoltaic Solar Energy Conference and Exhibition (EU PVSEC 2010) Proceedings, 2010, pp. 2078–2083, <https://doi.org/10.24406/publica-r-368902>.
- [18] K. Dornich, T. Hahn, J.R. Niklas, MRS Proc. 864 (2005) E11.2, <https://doi.org/10.1557/PROC-864-E11.2>.
- [19] N. Schüler, S. Anger, K. Dornich, J.R. Niklas, K. Bothe, Sol. Energy Mater. Sol. Cells 98 (2012) 245–252, <https://doi.org/10.1016/j.solmat.2011.11.017>.
- [20] B. Berger, N. Schüler, S. Anger, B. Gründig-Wendrock, J.R. Niklas, K. Dornich, Phys. Status Solidi A 208 (2011) 769–776, <https://doi.org/10.1002/pssa.201083994>.
- [21] K. Dornich, N. Schüler, B. Berger, J.R. Niklas, Mater. Sci. Eng. B 178 (2013) 676–681, <https://doi.org/10.1016/j.mseb.2012.11.014>.
- [22] IEEE standard test procedures for high-purity germanium crystals for radiation detectors, IEEE Std 1160-1993 (1993) 1–36, <https://doi.org/10.1109/IEEESTD.1993.115139>.
- [23] K.P. Gradwohl, A. Gybin, J. Janicskó-Csáthy, M. Roder, A.N. Danilewsky, R. R. Sumathi, J. Electron. Mater. 49 (2020) 5097–5103, <https://doi.org/10.1007/s11664-020-08260-1>.
- [24] O.A. Noghabi, M. Jomâa, M. M'hamdi, J. Cryst. Growth 362 (2013) 77–82, <https://doi.org/10.1016/j.jcrysgro.2011.10.062>.

- [25] J.C. Lambopoulos, C.N. Delametter, *J. Cryst. Growth* 92 (1988) 390–396, [https://doi.org/10.1016/0022-0248\(88\)90023-1](https://doi.org/10.1016/0022-0248(88)90023-1).
- [26] P.C. Palletti, P. Seyidov, A. Gybin, M. Pietsch, U. Juda, A. Fiedler, K. Irmscher, R. R. Sumathi, *J. Mater. Sci. Mater. Electron.* 35 (2024) 11814, <https://doi.org/10.1007/s10854-023-11814-8>.
- [27] T.T. Tran, J. Wong-Leung, L.A. Smillie, A. Hallén, M.G. Grimaldi, J.S. Williams, *APL Mater.* 11 (2023) 0146424, <https://doi.org/10.1063/5.0146424>.
- [28] K. Hauffe, Z. Elektrochem. Ber. Bunsenges. Phys. Chem. 65 (1961) 398, <https://doi.org/10.1002/bbpc.19610650426>.
- [29] R.N. Hall, T.J. Soltys, *IEEE Trans. Nucl. Sci.* 18 (1971) 160–165, <https://doi.org/10.1109/TNS.1971.4325857>.
- [30] J. Fernández, Development of Crystalline Germanium for Thermophotovoltaics and High-Efficiency Multi-Junction Solar Cells, Ph.D. thesis, Available at, <http://nbn-resolving.de/urn:nbn:de:bsz:352-203218>, 2010.
- [31] Ben G. Streetman, Sanjay Kumar Banerjee, Solid State electronic devices, Global Edition, 7th ed, Pearson Education, 2015. <https://elibrary.pearson.de/book/99.150005/9781292060767> (accessed July 1, 2025).
- [32] P. Śpiewak, K. Sueoka, J. Vanhellemont, K.J. Kurzydłowski, K. Mlynarczyk, P. Wabiński, I. Romandic, *Physica B* 401–402 (2007) 205–209, <https://doi.org/10.1016/j.physb.2007.08.147>.
- [33] M.C. Petersen, A.N. Larsen, A. Mesli, *Phys. Rev. B* 82 (2010) 075203, <https://doi.org/10.1103/PhysRevB.82.075203>.
- [34] B.G. Streetman, *J. Appl. Phys.* 37 (1966) 3145–3152, <https://doi.org/10.1063/1.1703176>.
- [35] S. Aryal, E.R. Batista, G. Wang, Effect of Group-V Impurities on the Electronic Properties of Germanium Detectors: An Insight from First-Principles Calculations. <http://arxiv.org/abs/2507.17676>, 2025.
- [36] E.E. Haller, G.S. Hubbard, W.L. Hansen, A. Seeger, In: International Conference on Radiation Effects in Semiconductors, Dubrovnik, Yugoslavia, 1976. <https://escholarship.org/uc/item/4s33g9sr> (accessed November 9, 2022).
- [37] M. Sande, L. Goethem, L. Laet, H. Guislain, *Appl. Phys. A Mater. Sci. Process.* 40 (1986) 257–261, <https://doi.org/10.1007/BF00616604>.
- [38] E. Simoen, P. Clauws, J. Vennik, *Solid State Commun.* 54 (1985) 1025–1029, [https://doi.org/10.1016/0038-1098\(85\)90752-5](https://doi.org/10.1016/0038-1098(85)90752-5).
- [39] W.W. Tyler, *J. Phys. Chem. Solids* 8 (1959) 59–65, [https://doi.org/10.1016/0022-3697\(59\)90274-4](https://doi.org/10.1016/0022-3697(59)90274-4).
- [40] M. Grundmann, Electronic defect states, in: *The Physics of Semiconductors*, Springer, 2016, pp. 203–253, [https://doi.org/10.1007/978-3-319-23880-7\\_7](https://doi.org/10.1007/978-3-319-23880-7_7).
- [41] C. Claeyns, E. Simoen, Germanium-based technologies, Elsevier (2007), <https://doi.org/10.1016/B978-0-08-044953-1.X5000-5>.
- [42] L.C. Kimerling, Compensation of Germanium by Radiation Defects. <http://hdl.handle.net/1721.1/13273>, 1969. (Accessed 8 September 2023).
- [43] Andreas Fiedler, Electrical and optical characterization of  $\beta$ -Ga<sub>2</sub>O<sub>3</sub>, Ph.D. thesis. <https://doi.org/10.18452/20958>, 2019.
- [44] G. Yang, H. Mei, Y.T. Guan, G.J. Wang, D.M. Mei, K. Irmscher, *J. Phys. Conf. Ser.* 606 (2015) 012013, <https://doi.org/10.1088/1742-6596/606/1/012013>.
- [45] P.P. Debye, E.M. Conwell, *Phys. Rev.* 93 (1954) 693–706, <https://doi.org/10.1103/PhysRev.93.693>.
- [46] P. Śpiewak, K. Sueoka, J. Vanhellemont, K.J. Kurzydłowski, K. Mlynarczyk, P. Wabiński, I. Romandic, *Physica B* 401–402 (2007) 205–209, <https://doi.org/10.1016/j.physb.2007.08.147>.
- [47] V.P. Markevich, I.D. Hawkins, A.R. Peaker, K.V. Emtsev, V.V. Emtsev, V. Litvinov, L.I. Murin, L. Dobaczewski, *Phys. Rev. B* 70 (2004) 235213, <https://doi.org/10.1103/PhysRevB.70.235213>.